

Synthesis and characterization of silver nanoparticle-anchored amine-functionalized mesoporous silica for electrocatalytic determination of nitrite

Piyush Kumar Sonkar · Vellaichamy Ganesan

Received: 10 September 2014 / Revised: 17 December 2014 / Accepted: 25 December 2014 / Published online: 10 January 2015
© Springer-Verlag Berlin Heidelberg 2015

Abstract This work describes an easy and simple method for the synthesis of silver nanoparticles (Ag Nps) incorporated amine-functionalized silica (AFS) and its utilization in the construction of an electrochemical sensor. Ag Np-incorporated AFS (Ag-AFS) is characterized by several methods including UV-vis, infrared (IR), and electrochemical techniques. Further, Ag-AFS material is coated on glassy carbon (GC) electrode and utilized for the electrocatalytic oxidation of NO_2^- . The oxidation current of NO_2^- varies linearly from 1.0 to 16,000.0 μM , and the detection limit is 0.07 μM with the sensitivity of 0.43 $\mu\text{A } \mu\text{M}^{-1} \text{cm}^{-2}$. This new material exhibits a broad linear range, low detection limit, high sensitivity, selectivity, and stability for NO_2^- determination. Remarkably, the Ag-AFS is utilized for the quantitative determination of NO_2^- in fresh spinach samples.

Keywords Silver nanoparticles · Electrocatalysis · Amine-functionalized silica · Nitrite oxidation

Introduction

Recently, metal nanoparticles (Nps) become a promising area of research for many scientists due to their wide range of applications in several fields like material science, optics, microelectronics, energy storage, medicine, catalysis, and

chemical/biosensors [1–5]. The properties of Nps are governed by size, shape, and synthetic route through which they are prepared and type of stabilizer used [4, 5]. Silver Nps (Ag Nps)-based electrochemical sensors have been realized to be a stimulating area of research since they show promising applications [3, 6–16]. Their large surface area makes them as effective catalyst for several chemical and biological reactions such as hydrogen peroxide oxidation [13] and reduction [14], bromate reduction [15], glucose oxidation [16], and nitrite (NO_2^-) oxidation [6–11].

Mesoporous MCM-41-type silica possesses nano-sized pores ranging from 2 to 50 nm and displays various applications in the field of electrocatalysis as well as in materials science [8, 12, 17–30]. Functionalized mesoporous silica materials due to their high surface area and strong adsorption characteristics exhibit excellent properties of a catalyst and/or catalyst support [8, 12, 17, 19, 24–26]. Functionalization of MCM-41-type silica by mercaptopropyl or propylamine creates a way to anchor Ag Nps inside the channels of the silica. Such functionalization increases the stability of metal Nps and decreases their agglomeration [8, 12, 17–19, 24–26].

Electrochemical determination of NO_2^- is significant due to its environmental- and biological-related issues [6–12, 31–37]. NO_2^- is frequently found in fertilizers, corrosion inhibitors, industrial waste water, detergents, and food additives [31, 32]. Excess NO_2^- pollutes environment and has toxic effects for human health. NO_2^- is a precursor for carcinogenic nitrosamine, and high concentration of NO_2^- in human body increases the irreversible oxidation of hemoglobin to methemoglobin [33, 34]. Therefore, there is an increasing demand for efficient NO_2^- sensors and effective NO_2^- removal methods [6–12, 33–35, 37]. Ag Np-incorporated mercaptopropyl-functionalized MCM-41-type materials for NO_2^- [8] and Au Np-incorporated MCM-41 for uric acid and ascorbic acid determinations [19] are recently reported

Electronic supplementary material The online version of this article (doi:10.1007/s10008-014-2725-3) contains supplementary material, which is available to authorized users.

P. K. Sonkar · V. Ganesan (✉)
Department of Chemistry, Faculty of Science, Banaras Hindu
University, Varanasi 221 005, UP, India
e-mail: velganes@yaho.com

from our research group. However, in most of the cases, the sizes of the NPs vary to a large extent because of the utilization of external reducing agents for the reduction of the metal ions [8, 19]. In the present work, we did not use any external reducing agents, and therefore, it is expected to obtain uniform-sized Ag Nps with even distribution throughout the material. Using this new and improved material (denoted as Ag-amine-functionalized silica (AFS), *vide infra*) in this work, efficient electrocatalytic oxidation of NO_2^- is realized and utilized for the sensitive NO_2^- determination.

Experimental

Apparatus Images from atomic force microscopy (AFM) were recorded using NOVA-MDT (Russia) microscope. Electrochemical experiments were carried out on a CH Instruments (CHI-660C, USA) electrochemical workstation. Transmission electron microscope (TEM) images and selected area electron diffraction (SAED) were collected from TECNAI 20G² FEI microscope (at 120 kV). Absorbance spectra of solid samples were recorded from UV-vis spectrophotometer (UV 1700 PharmaSpec, Shimadzu) [38]. Infrared (IR) spectra were recorded from IR spectrometer (PerkinElmer, spectrum 2 UK). SEM images with energy-dispersive X-ray analysis (EDAX) were obtained from SEM-VEGA 3 TESCAN with EDAX (Bruker) instrument. Thermogravimetric analysis (TGA) was done on a thermogravimetric analyzer (PerkinElmer STA 6000, Netherlands) with a heating rate of $10\text{ }^\circ\text{C min}^{-1}$ under nitrogen atmosphere. Powder X-ray diffraction (XRD) patterns were collected from classical powder diffractometer (I-D 3000 SEIFERT, Germany).

Chemicals and reagents Aminopropyltrimethoxysilane (APTMS), tetraethoxysilane (TES, >98 %), and cetyltrimethylammonium bromide (CTAB) were purchased from Sigma-Aldrich. Silver nitrate is purchased from Merck and polyvinyl alcohol (PVA) from SD Fine, India. Phosphate-buffered solution (PBS) was prepared from potassium dihydrogen orthophosphate (KH_2PO_4) and dipotassium hydrogen orthophosphate (K_2HPO_4). Other reagents were of analytical grade and used as received. Triple-distilled water was used for synthesis and other experimental needs. AgOH was prepared by adding 0.1-M AgNO_3 aqueous solution to 0.1-M NaOH solution. Formed precipitate was filtered, washed with excess water, dried, powdered, and used for UV-vis analysis.

Synthesis of amine-functionalized silica AFS was synthesized similar to a literature procedure [18]. CTAB (4.8 g) was added to distilled water (100 mL) and 90 mL ethanol in which 29.2 mL of 25 % aqueous ammonia was added. The precursor mixture was prepared by dissolving APTMS and TES in 20:80 molar ratio in 10 mL ethanol; then, this solution was

added to the surfactant solution and vigorously stirred. The reaction mixture was kept under stirring for 2 h. Formed product was filtered and washed with excess ethanol and water. White powdered sample obtained from filtration was vacuum-dried for 24 h. The surfactant was removed by extraction in HCl-ethanol mixture under refluxing conditions for 18 h [8, 12, 17–20, 24, 25]. The reaction mixture was filtered, washed with ethanol, and kept in vacuum for 24 h.

Synthesis of Ag Np-incorporated AFS Here, a simple and new approach is used for reduction of Ag^+ ions and immediate anchoring of the formed product, Ag Nps, into the pores of AFS. Typically, aqueous AgNO_3 solution (30 mL of 1.0 mM) was equilibrated with 0.3 g of AFS under stirring and dark conditions at room temperature for 96 h. Subsequently, the product was filtered and washed with excess of water. The resulting Ag Np-anchored AFS (Ag-AFS) was dried under vacuum for 24 h. It is worth to mention here that this procedure is different from our previous reports for the synthesis of Ag or Au Nps into MCM-41-type materials [8, 12, 17, 19, 21–25]. Since the present method does not utilize any external reducing agents and the amine groups are projected into the channels of AFS, uniform distribution of Ag Nps inside the channels of the AFS is obtained. This uniformity in distribution of Ag Nps and the presence of Ag Nps inside the channels of AFS will improve charge and/or ion transport properties between bulk electrode and solution which is essential for an efficient electrocatalytic process.

Preparation of electrochemical sensing platform Films of Ag-AFS material prepared on glassy carbon (GC) electrodes serve as the electrochemical sensing platforms [8, 12, 17, 19, 24, 25]. Surface of the GC electrodes were cleaned by polishing on a Buehler-felt pad with wet alumina powder. The electrodes were further washed with water, sonicated for 5 min in distilled water, and dried in air under room conditions. Aqueous colloid of 1.0 % Ag-AFS (or AFS for blank) was prepared with 0.01 % PVA as a binder. Five microliters of the colloid was drop-coated on the GC electrode surface. The electrode was air-dried in the dark and used for electrochemical studies within 36 h. Depending upon the material coated on the electrode, the sensing platform is represented as GC/AFS or GC/Ag-AFS.

Result and discussion

IR and UV-vis interpretations AFS and Ag-AFS exhibit characteristic vibrations as shown in Fig. 1. AFS exhibits a peak at 1104 cm^{-1} for Si–OH vibration. This peak is shifted to 1097 cm^{-1} due to interaction of Ag Nps with silanol groups in the Ag-AFS material [26]. The peak observed at 1632 cm^{-1} is mainly from bending vibration of adsorbed water and a broad

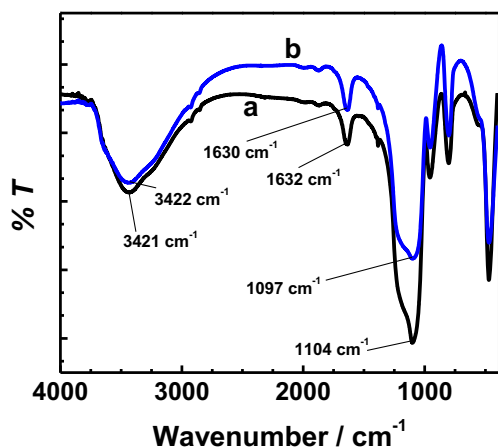


Fig. 1 FTIR spectra of AFS (a) and Ag-AFS (b)

peak at 3421 cm^{-1} due to $-\text{OH}$ group present in AFS [27]. Generally, $-\text{CN}$ group exhibits about $1000\text{--}1200\text{ cm}^{-1}$; however, this peak is not resolved due to overlapping of Si-O-Si stretching and Si-CH_2 stretching in the region $1200\text{--}1250\text{ cm}^{-1}$ [28, 39]. The major shift in Si-OH of Ag-AFS indicates the successful incorporation of Ag Nps into AFS [6, 8, 40].

Ag-AFS shows characteristic orange-yellow color due to surface plasmon resonance of Ag Nps [41, 42]. Size and shape characteristics of Ag Nps lead to red or blue shift in absorbance due to increase or decrease of particle size, respectively [3]. Spherical-shaped Ag Nps generally shows absorbance in the range $400\text{--}440\text{ nm}$ [7, 8, 43]. In this work, Ag-AFS displays broad absorption peak centered around 421 nm while AFS does not show any characteristic peak in this region (Fig. 2). The presence of this broad band centered at 421 nm specifies the existence of Ag Nps in the Ag-AFS material. To rule out the presence of AgOH in the synthesized Ag-AFS, spectrum of AgOH is also shown (Fig. 2c). As AgOH exhibits peak at different wavelength (376 nm) than Ag-AFS, it is concluded that the band observed at 421 nm in Ag-AFS is due to Ag Nps only. According to previous studies, prism-shaped Ag Nps

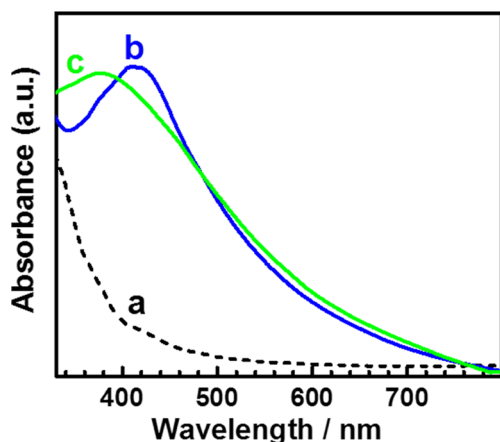


Fig. 2 UV-vis absorbance spectra of AFS (a), Ag-AFS (b), and AgOH (c)

show two bands around 335 and 770 nm [44], while rod-shaped Ag Nps display band around $380\text{--}400\text{ nm}$ [45]. These results suggest that the prepared Ag Nps are spherically shaped with an approximate size of $5\text{--}40\text{ nm}$. The above results were further supported by TEM analysis (vide infra).

X-ray diffraction characterizations Powder XRD patterns of AFS and Ag-AFS materials are recorded in the 2θ range of 10 to 80° (Fig. 3). The peak that arises at 23° is the characteristic of wormhole-like mesostructures of organosilica [8, 21–23]. The additional peaks present in Ag-AFS (Fig. 3b) at 2θ values, 38.3 , 43.5 , 63.9 , and 77.0° , are the characteristics of (111), (200), (220), and (311) planes of the Ag face-centered cubic crystals [8, 46]. The presence of these peaks represents that Ag exists in metallic state in Ag-AFS material.

SEM, TEM and AFM analyzes SEM images (Fig. 4) of AFS and Ag-AFS display sphere-shaped silica materials usually obtained in this synthetic route [8, 12, 17, 18, 20–25, 31]. Presence of Ag Nps in Ag-AFS did not show any distinct difference between AFS and Ag-AFS (Fig. 4) though it is expected that the immobilization of Ag Nps on the surface of the silica material can decrease the average smoothness and enhance the average roughness of the Ag-AFS [46, 47]. TEM images of AFS and Ag-AFS with SAED are recorded and shown in Fig. 5. The pores of AFS and Ag-AFS are clearly visible in the TEM images. Ag-AFS shows distinct dark black spherical spots on the surface of the silica material due to Ag Nps. Particle size of Ag Nps varies from 5 to 40 nm with nearly spherical in shape and displays uniform distribution throughout the Ag-AFS. Diffraction ring patterns observed in SAED of Ag-AFS represent the crystalline nature of Ag Nps [3, 8, 48]. Signal observed in EDAX for Ag provides evidence for the presence of Ag in the AFS material (Fig. S-1, supplementary information). AFM images of AFS and Ag-AFS films are recorded and shown in Fig. 6. Ag-AFS films are compact and misted as compared to AFS films indicating the incorporation of Ag

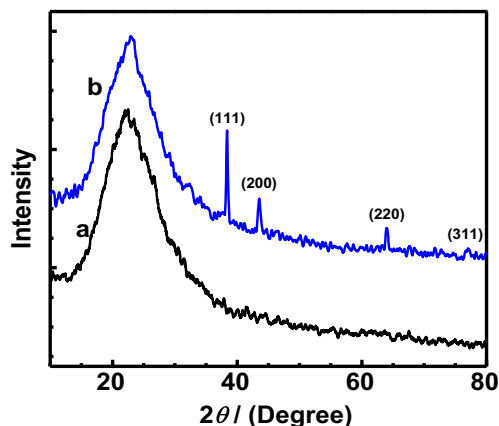
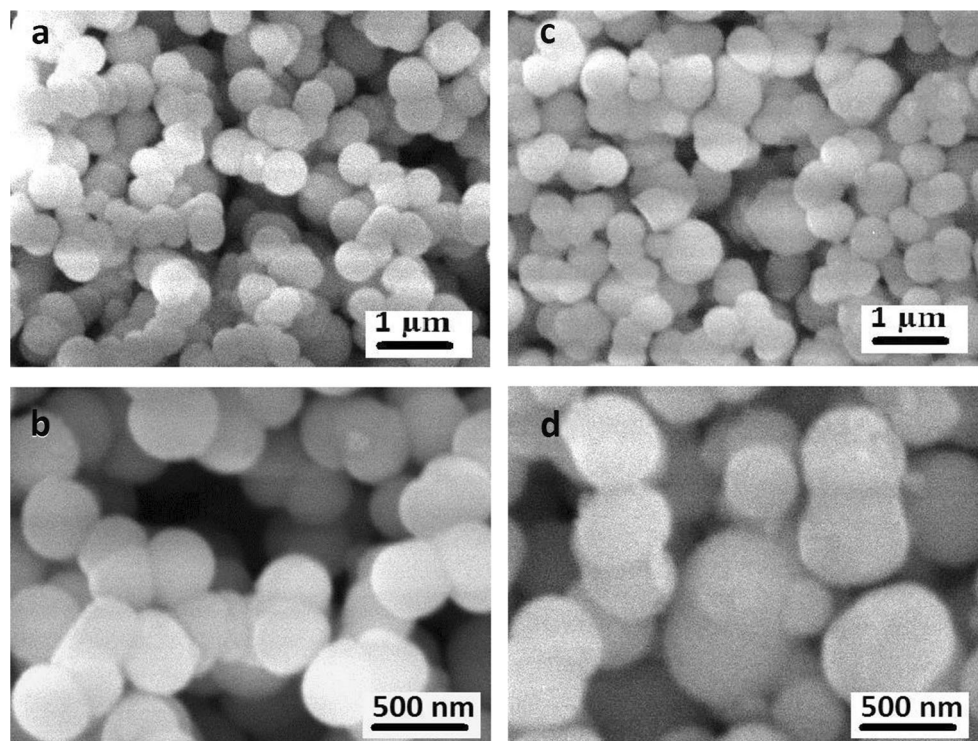


Fig. 3 Powder XRD patterns of AFS (a) and Ag-AFS (b)

Fig. 4 SEM images of AFS (a, b) and Ag-AFS (c, d) at different magnifications



Nps [49]. AFS spheres appear as granular and smooth while Ag-AFS exhibits coarse granular-type structures. The root-mean-square (rms) roughness for AFS (70.4 nm) was increased due to the dispersion of Ag Nps into/onto the AFS in Ag-AFS (78.6 nm) [29, 30, 50, 51].

Thermogravimetric analysis TGA was performed in nitrogen atmosphere with a heating rate of $10\text{ }^{\circ}\text{C min}^{-1}$ (Fig. 7). A loss of 8–9 % of original weight was observed at $100\text{ }^{\circ}\text{C}$ due to loss of adsorbed water [52] in both AFS and Ag-AFS samples. Further, a steady and slow weight loss is observed between 200 and $600\text{ }^{\circ}\text{C}$ representing very less condensation of silanol groups at the surface of AFS and Ag-AFS [53]. Above $370\text{ }^{\circ}\text{C}$, further significant decrease was observed probably due to the decomposition of bonded organosilane (aminopropyl) moieties from the silica material [54]. However, incorporation of Ag Nps into AFS reduces the percentage thermal weight loss and consequently increases the

thermal stability of Ag-AFS which is clearly demonstrated from this study.

Characterization of the sensing platform Cyclic voltammetry (CV) of Ag-AFS-coated GC electrode is studied in 0.1 M pH 7.0 PBS in the potential range -0.6 to 0.8 V at different scan rates (Fig. 8). Ag-AFS films show characteristic redox peaks at 0.29 and -0.04 V (50 mVs^{-1}) due to oxidation (Ag^0 to Ag^+) and reduction (Ag^+ to Ag^0) process [8]. On increasing the scan rate, the oxidation peak potential gradually decreases. For example, at a scan rate of 50 mVs^{-1} , the oxidation peak is observed at 0.29 V whereas at a scan rate of 500 mVs^{-1} , the oxidation peak is observed at 0.25 V . This small decrease in peak potential on increasing scan rate may be due to the sluggish redox process at the GC/Ag-AFS. The reduction peak at -0.04 V is less intense and ill-defined at low scan rates; however, at high scan rates, the current increases with a defined peak. Repetitive cycles of GC/Ag-AFS (five cycles) at a scan

Fig. 5 TEM images of AFS (a) and Ag-AFS (b) with corresponding SAED in the inset

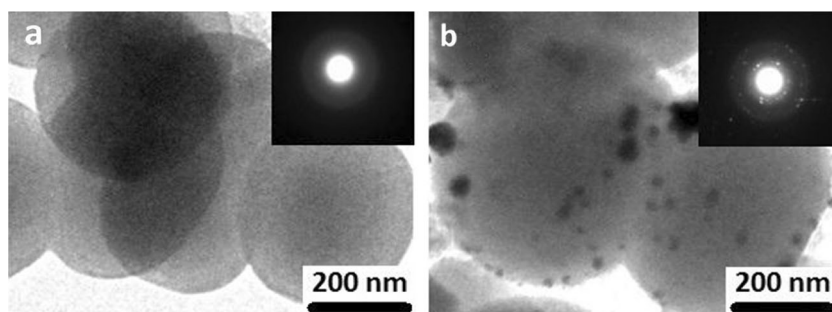
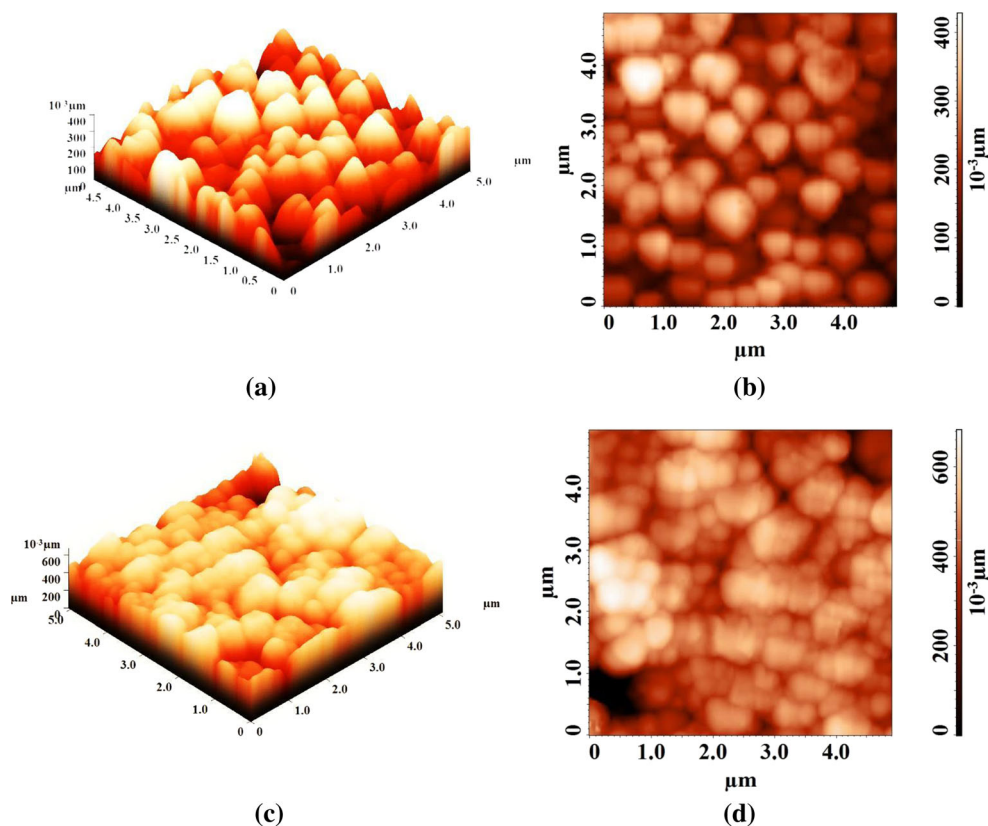


Fig. 6 The 3-D (a, c) and 2-D (b, d) AFM images of AFS (a, b) and Ag-AFS (c, d)



rate of 50 mVs^{-1} are shown in Fig. S-2, supplementary information. A very small shift in peak potential (2 mV) is observed from the first cycle to the second cycle. The rest of the cycles represent very less or negligible change in the peak potential. Very less or negligible change in peak current on the repetitive cycles indicates that no or negligible amount of Ag^+ is leached into the supporting electrolyte solution which is also not reduced back to electrode as Ag^0 . A graphical interpretation of anodic and cathodic peak currents (I_{pa} and I_{pc} , respectively), with square root of scan rate ($\nu^{1/2}$) at high scan rates ($50\text{--}500 \text{ mVs}^{-1}$), shows linear relationship (inset of Fig. 8) which

signifies the diffusion-controlled process at the sensing platform [6, 55, 56].

Kinetics of NO_2^- oxidation at the sensing platform Incremental addition of NO_2^- at Ag-AFS sensing platform shows a linear increase in the catalytic current due to electrocatalytic oxidation of NO_2^- [36, 40, 55]. Increase in oxidation peak potential (E_{pa}) with increase in scan rate reveals the irreversible oxidation (or lethargic oxidation) of NO_2^- at GC/Ag-AFS [8]. For irreversible electrocatalytic oxidation, the slope which can be

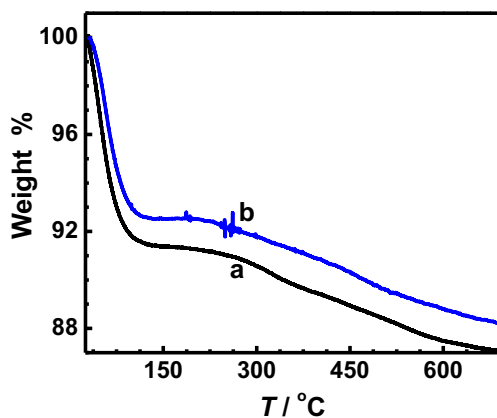


Fig. 7 TGA plot for AFS (a) and Ag-AFS (b) from 25 to 700 °C at the rate of $10 \text{ }^\circ\text{C min}^{-1}$ in nitrogen atmosphere

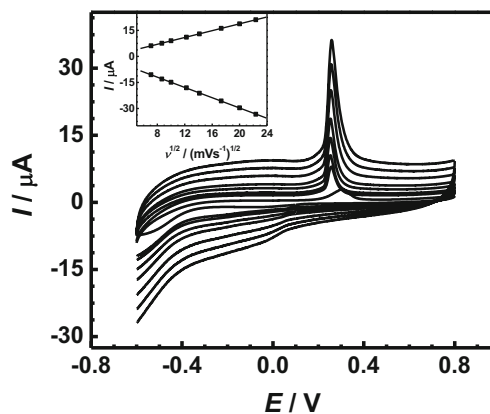


Fig. 8 Cyclic voltammograms of GC/Ag-AFS (from -0.6 to 0.8 V) at scan rates of $50, 75, 100, 150, 200, 300, 400,$ and 500 mVs^{-1} in $0.1 \text{ M pH } 7.0 \text{ PBS}$. Inset represents linearity of anodic and cathodic peak currents with square root of scan rate, $\nu^{1/2}$

obtained from E_{pa} vs. $\log(\nu)$ plot (Fig. S-3, supplementary information) can give useful information about the rate-determining step (Eq. (1)).

$$E_{pa} = \frac{[b \log(\nu)]}{2} + \text{constant} \quad (1)$$

where the value of b is $2.303RT/((1-\alpha)n_{\alpha}F)$. The other terms, E_{pa} , α , n_{α} , and ν , are the anodic peak potential for NO_2^- oxidation, transfer coefficient, number of electrons involved in rate-limiting step, and scan rate, respectively. The b value is found to be 122 mV from calculation which is near to the reported value [56].

One can calculate the number of electrons involved in the oxidation process from the slope of I_p vs. $\nu^{1/2}$ plot (Fig. S-4, supplementary information) using Eq. (2).

$$I_p = 2.99 \times 10^5 n [(1-\alpha)n_{\alpha}]^{1/2} C_0 D^{1/2} A \nu^{1/2} \quad (2)$$

where D is the diffusion coefficient and C_0 is the bulk concentration of NO_2^- . The value of n is found to be 1.65 using a D value of $2.1 \times 10^{-5} \text{ cm}^2 \text{ s}^{-1}$ [57] which indicates a two-electron transfer process.

Chronoamperometry is performed at Ag-AFS sensing platform in 0.1 M pH 7.0 PBS with different additions of NO_2^- . The catalytic rate constant is found to be $0.49 \times 10^5 \text{ M}^{-1} \text{ s}^{-1}$ employing Eq. (3).

$$\frac{I_{cat}}{I_L} = (\pi t)^{1/2} (k_{cat} C_0)^{1/2} \quad (3)$$

where I_{cat} and I_L are the currents obtained from chronoamperogram in the presence and absence of nitrite, respectively.

Further, D is determined for NO_2^- according to the Cottrell equation (Eq. (4)). The data obtained from chronoamperometry with increasing additions of NO_2^- was used for the preparation of the plot, I_p vs. $t^{-1/2}$. Using the slope of the linear line, D value is calculated to be $5.09 \times 10^{-5} \text{ cm}^2 \text{ s}^{-1}$ which is near to the reported value [56–58].

$$I = nFD^{1/2}AC_0\pi^{-1/2}t^{-1/2} \quad (4)$$

Electrocatalytic oxidation of NO_2^- Ag-AFS sensing platform is used for electrocatalytic oxidation of NO_2^- . GC/Ag-AFS electrode shows characteristic peak at 0.29 V (at a scan rate of 20 mVs^{-1}) while GC/AFS electrode does not show any characteristic peak in the same region (-0.6 to 1.2 V). Upon addition of 0.5 mM NO_2^- to GC/AFS, the current increases to some extent, while large increase in current is observed with considerable decrease in the NO_2^- oxidation peak potential at the GC/Ag-AFS electrode [7] (Fig. 9). Every addition of NO_2^- increases the oxidation current (Fig. S-5, supplementary information), suggesting the efficient electrocatalytic process for the

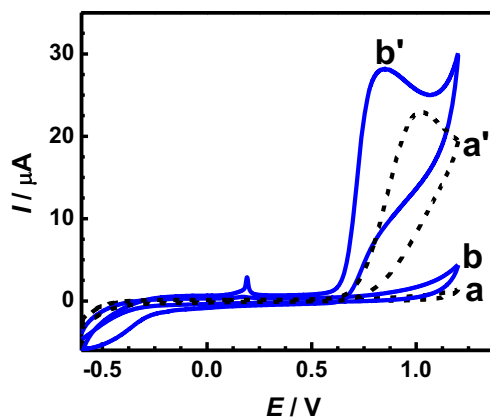


Fig. 9 Cyclic voltammograms of GC/AFS (*a, a'*) and GC/Ag-AFS (*b, b'*) without (*a, b*) and with 0.5 mM NO_2^- (*a', b'*) at a scan rate of 20 mVs^{-1}

oxidation of NO_2^- . To utilize this property for the determination of NO_2^- , the obtained calibration plot with error bars is shown in Fig. 10. The calibration plot shows two segmented linear lines from 1.0 to $450.0 \mu\text{M}$ and from 450.0 to $16,000.0 \mu\text{M}$. Addition of NO_2^- above $16,000.0 \mu\text{M}$ shows very little increase in current (not shown in Fig. 10) which indicates that the catalytic sites in Ag-AFS sensing platform are saturated (or slowly regenerated) because of high concentrations of NO_2^- . Inset of Fig. 10 represents the enlarged view of the calibration plot for the first linear range (from 1.0 to $450.0 \mu\text{M}$). A decrease in slope is observed in the calibration plot for high concentration (450.0 to $16,000.0 \mu\text{M}$) of NO_2^- . The increased slope at low concentration of NO_2^- may be due to increased amount of complex formation between NO_2^- and Ag Nps up to a certain level of NO_2^- concentration ($450.0 \mu\text{M}$). After that, saturation of catalytic site starts to occur and the decrease in slope of calibration plot is observed [1, 8, 42].

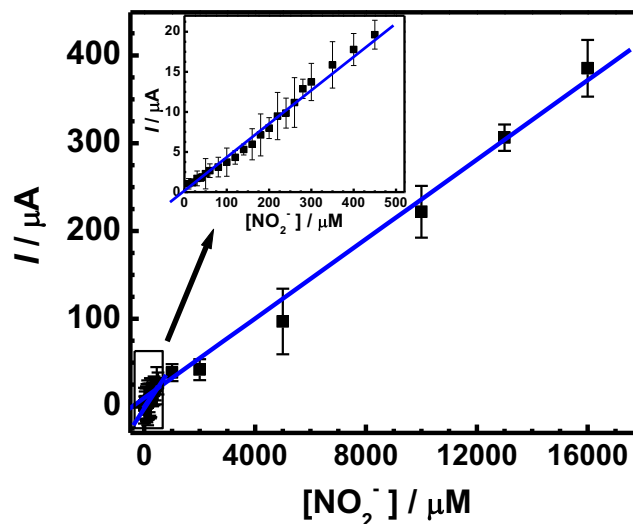


Fig. 10 Calibration plot with error bars for GC/Ag-AFS with different additions of NO_2^- from 1.0 to $16,000.0 \mu\text{M}$ in $0.1 \text{ M pH } 7.0$ PBS at a scan rate 20 mVs^{-1} . Inset represents the expanded view of calibration plot from 1.0 to $450.0 \mu\text{M}$ of NO_2^-

Table 1 A comparison of efficiency of different modified electrodes toward the electrocatalytic oxidation and subsequent determination of NO_2^-

Electrode	Potential	pH	Linear range (μM)	Detection limit (μM)	Sensitivity	References
Ag-P(MMA-co-AMPS)-modified GCE	0.9 ^a	7.0	1–100,000	0.2	104.6 $\mu\text{A } \mu\text{M}^{-1} \text{ cm}^{-2}$	Rastogi et al. [6]
GC/Nf/Fe(bpy) ₃ ²⁺	0.9 ^a	7.0	200–20,000	–	–	Azad and Ganesan [7]
Ag-NEE-modified GCE	0.92 ^a	7.0	10–300	–	–	Pal and Ganesan [8]
GR-MWCNT/FeNP nanocomposite	0.77 ^b	5.0	0.1–1680	0.076	0.697 $\mu\text{A } \mu\text{M}^{-1} \text{ cm}^{-2}$	Etienne et al. [18]
Poly(toluidine blue)	1.10 ^a	3.0	0.1–15.2	0.05	0.47 $\mu\text{A } \mu\text{M}^{-1} \text{ cm}^{-2}$	Rastogi et al. [6]
CuO graphite composite electrode	0.98 ^a	–	100–1250	0.60	–	Sljukic et al. [62]
Thionine-modified ACNT electrode	0.80 ^b	3.5	3–500	1.12	–	Zhao et al. [63]
PEDOT/GR-modified GCE	0.7 ^a	6.0	0.3–600	0.1	0.13 $\mu\text{A } \mu\text{M}^{-1}$	Nie et al. [64]
GC/H ⁺ -bt/Fe(phen) ₃ ²⁺	0.98 ^a	7.0	1–100,000	1.0	–	Azad et al. [65]
GC/Na ⁺ -bt/Fe(phen) ₃ ²⁺	0.95 ^a	7.0	1–100,000	1.0	–	
CR-GO-modified GCE	0.80 ^b	5.0	8.9–167	1.02	0.0267 $\mu\text{A } \mu\text{M}^{-1}$	Mani et al. [66]
Au/Fe(III) nanoparticle-modified GCE	0.73 ^a	5.0	0.3–150	0.2	–	Liu et al. [9]
MnO ₂ nanorod-modified GCE	0.90 ^a	7.0	0.29–26 090	0.29	0.0012 $\mu\text{A } \mu\text{M}^{-1}$	Feng et al. [67]
GC/Ag-AFS	0.92 ^a	7.0	1–16,000	0.07	0.43 $\mu\text{A } \mu\text{M}^{-1} \text{ cm}^{-2}$	This work

P(MMA-co-AMPS) copolymer of methyl methacrylate (MMA) and 2-acrylamido-2-methylpropane sulfonic acid (AMPS), Nf/Fe(bpy)₃²⁺ Nafion iron bipyridyl, Ag-NEEs Ag-nanoelectrode ensembles, GR-MWCNTs/FeNPs iron nanoparticle decorated graphene-multiwalled carbon nanotube nanocomposite, ACNTs aligned carbon nanotubes, PEDOT/GR poly(3,4-ethylenedioxythiophene)/graphene nanocomposite, H⁺-bt H⁺-exchanged bentonite, Fe(phen)₃²⁺ tris(1,10-phenanthroline) iron(II), Na⁺-bt Na⁺-exchanged bentonite, CR-GO chemically reduced graphene oxide, GCE glassy carbon electrode

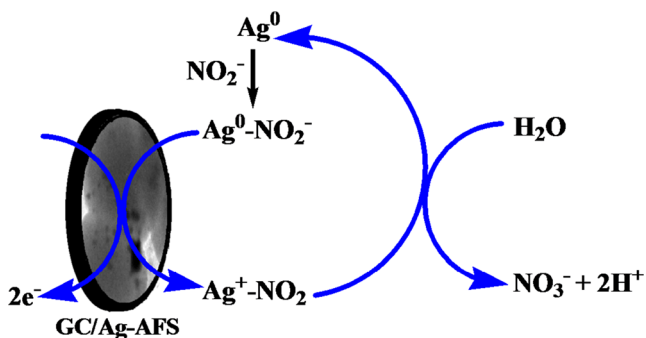
^a Saturated calomel electrode

^b Ag/AgCl electrode

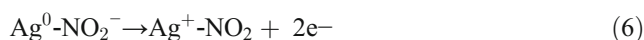
The detection limit and sensitivity for the determination of NO_2^- at Ag-AFS sensing platform are found to be 0.07 μM (or 0.003 mg/L) and 0.43 $\mu\text{A } \mu\text{M}^{-1} \text{ cm}^{-2}$, respectively. According to World Health Organization (WHO) recommendation, tolerance limit of NO_2^- for drinking water is 0.05 to 5 mg/L [59, 60]. Therefore, this sensing platform could be useful for determination of NO_2^- in drinking water far below than the recommended level. Advantages and comparative assessment of this new sensing platform, Ag-AFS, over other materials/methods can be evaluated from Table 1 [6–9, 18, 56, 61–67]. It is clear from Table 1 that Ag-AFS shows broad calibration range, low detection limit, and high sensitivity than

those of many other reported works (including our previous reports using Ag Np-incorporated polymer nanocomposite or mercaptopropyl-functionalized silica [6, 14]).

Mechanism for electrocatalytic oxidation of nitrite The mechanism for electrocatalytic oxidation of NO_2^- is expected to occur similar to the reported studies [6, 8] in which NO_2^- is oxidized to NO_3^- . Briefly, the Ag^0 originally present in Ag-AFS forms a complex in the presence of NO_2^- ($\text{Ag}^0\text{-NO}_2^-$). This complex is electrochemically oxidized to $\text{Ag}^+\text{-NO}_2$ (or Ag^+ and NO_2) (peak around 0.19 V). In the next step, it is converted to Ag^0 and NO_3^- (peak around 0.92 V). These processes (Eqs. (5)–(7)) are schematically shown in Scheme 1.



Scheme 1 Schematic representation indicating the electrocatalytic oxidation of NO_2^- at GC/Ag-AFS



However, it should be noted that the proposed mechanism (or complete mechanism) and the exact nature of species involved in the reactions require further study and the main aim

Table 2 Effect of different interfering species on the peak current of GC/Ag-AFS sensing platform for NO_2^- determination ($[\text{NO}_2^-]=1.0 \times 10^{-5}$ M and [interferents] 1×10^{-3} M)

Interferents	Signal change (%)	Interference
NaCl	-3.6	Negligible
NaClO_4	-9.2	Moderate
KCl	-5.2	Moderate
NH_4Cl	-6.0	Moderate
MgSO_4	+6.2	Moderate
NaNO_3	-7.4	Moderate
$\text{Zn}(\text{CH}_3\text{COO})_2$	-4.2	Negligible
CaCl_2	+8.2	Moderate
Urea	-4.1	Negligible
Oxalic acid	+9.6	Moderate
Glucose	+2.9	Negligible

Range of interference 0–5 % = no interference, 5–10 % = moderate interference, >10 % = serious interference

of this work is to exemplify the use of such mesoporous materials in the analytical applications.

Interference study Selectivity of GC/Ag-AFS toward the determination of NO_2^- is verified by interference study. Presence of 100-fold excess of possible interfering ions such as NaCl, KCl, NH_4Cl , MgSO_4 , NaNO_3 , and $\text{Zn}(\text{CH}_3\text{COO})_2$ did not affect the response of the electrode considerably. Physiological-related molecules such as glucose and urea also did not alter the signal considerably. A moderate interference is observed for NaClO_4 (-9.2 %), CaCl_2 (+8.2 %), and oxalic acid (+9.6 %). The interference of different ions in the determination of NO_2^- is summarized in Table 2. These results suggest that the Ag-AFS sensing platform has high selectivity for NO_2^- recognition even in the presence of 100-fold excess of possible common interfering ions and molecules [7].

Stability and reproducibility of the ESP GC/Ag-AFS demonstrates remarkable stability in neutral aqueous solutions, and it does not alter the redox peak current considerably even after several scans. Current obtained at 0.92 V is not changed even after several different determinations (the relative standard deviation (RSD) is 3.4 % for three repeated experiments).

Repeatability of GC/Ag-AFS is further analyzed with three different electrodes for the electrocatalytic oxidation of NO_2^- in 0.1 M pH 7.0 PBS. Oxidative current for NO_2^- was recorded with an interval of 1 min between the scans for three different electrodes. The current obtained at 0.92 V for NO_2^- oxidation at these three different electrodes shows very small change with a RSD of 3.6 % (three repeated experiments from each electrode). The electrochemical behavior and sensitivity are consistent (99 %) even after storing the electrodes (under normal room conditions) for 10 days (Fig. S-6, supplementary information). Therefore, GC/Ag-AFS electrodes can be used repeatedly for NO_2^- determination [48, 68].

Analysis of real sample NO_2^- present in spinach sample (source: Varanasi, India) is determined using this new Ag-AFS sensing platform. Typically, 100 g of spinach is grained to paste using a mixer/blender. The resulting paste/cream was transferred to a beaker and diluted to 250 mL with distilled water. The mixture was then dispersed well and centrifuged at 6000 rpm for 10 min. Supernatant was filtered, and the filtrate was directly used as a sample for the NO_2^- determination. The amount of NO_2^- in the spinach sample determined by the CV technique is found to be 11.3 mg/kg. Previous studies indicate that average amount of NO_2^- in the spinach sample varies from 3 to 15 mg/kg [30, 69]. It indicates that this new method is significant for the determination of NO_2^- concentration in the spinach sample. Further, the sample is spiked with standard solution of NO_2^- and gives a recovery of about 93–97 %. The recovery results are summarized in Table 3.

Conclusion Ag Nps are synthesized successfully by simple method without using any external reducing agents. The prepared Ag-AFS material exhibits electrocatalytic properties for NO_2^- oxidation by lowering the overpotential and increasing the catalytic current. The modified electrode, GC/Ag-AFS, shows broad calibration range, high stability, reproducibility high sensitivity, and low interference. The proposed sensor is successfully used for the determination of NO_2^- in the real sample (spinach) and provides satisfactory results. Ag-AFS material can be useful for development of cheap and effective NO_2^- electrochemical sensor for analysis of chemical and biological samples. This material is expected to be useful in

Table 3 Analysis of spinach sample (source: Varanasi, India) for NO_2^- determination

NO_2^- concentration (mg/kg)			Recovery (mg/kg)	Recovery %	RSD% (n=3)
Spinach	Standard added	Total			
11.3 (experimental average of three analyses)	0	11.3	–	–	5.09
	57.5	68.8	54.2	92.9	6.25
	115.2	126.5	117.3	93.1	1.77
	230.4	241.7	234.8	97.3	4.56

the oxidative removal of NO_2^- from polluted environmental resources.

Acknowledgments Substantial funding from UGC and CSIR, New Delhi, India, is acknowledged. PKS gratefully acknowledges UGC for RGNF. We are grateful to Prof. ON Srivastava, Banaras Hindu University, for TEM analysis and Dr. SA John, Gandhigram Rural University, for SEM studies.

References

- Zhang Y, Zhao Y, Yuan S, Wang H, He C (2013) *Sensors Actuators B* 185:602–607
- Li Y, Zhou Y, Xian H, Wang L, Huo J (2011) *Anal Sci* 27:1223–1228
- Jebakumar TN, Edison I, Sethuraman MG (2013) *Sustain Chem Eng* 1:1326–1332
- Tominaga M, Shimazoe T, Nagashima M, Taniguchi I (2008) *J Electroanal Chem* 615:51–61
- Wang G, Wang W, Wu J, Liu H, Jiao S, Fang B (2009) *Microchim Acta* 164:149–155
- Rastogi PK, Ganesan V, Krishnamoorthi S (2014) *J Mater Chem A* 2:933–943
- Azad UP, Ganesan V (2010) *Chem Commun* 46:6156–6158
- Pal M, Ganesan V (2010) *Analyst* 135:2711–2716
- Liu TS, Kang TF, Lu LP, Zhang Cheng SY (2009) *J Electroanal Chem* 632:197–200
- Lei J, Ju H, Ikeda O (2004) *J Electroanal Chem* 567:331–338
- Sunohara S, Nishimura K, Yahikozawa K, Ueno M, Enyo M, Takasu Y (1993) *J Electroanal Chem* 354:161–171
- Pal M, Ganesan V (2010) *Electrochim Acta* 55:4071–4077
- Azadbakht A, Abbasi AR, Gholivand MB, Derikvand Z (2014) *J Inorg Organomet Polym* 24:573–581
- Welch CM, Banks CE, Simm AO, Compton RG (2005) *Anal Bioanal Chem* 382:12–21
- Li Q, Zhang Q, Ding L, Zhou D, Cui H, Wei Z, Zhai J (2013) *J Chem Eng* 217:28–33
- Tominaga M, Shimazoe T, Nagashima M, Kusuda H, Kubo A, Kuwahara Y, Taniguchi I (2006) *J Electroanal Chem* 590:37–46
- Pal M, Ganesan V (2009) *Langmuir* 25:13264–13272
- Etienne M, Lebeau B, Walcarius A (2002) *New J Chem* 26:384–386
- Gupta R, Ganesan V (2014) *Colloids Surf B: Biointerfaces* submitted
- Gaslain FOM, Cyril D, Walcarius A, Lebeau B (2009) *J Sol-gel Sci Technol* 49:112–124
- Ganesan V, Walcarius A (2004) *Langmuir* 20:3632–3640
- Walcarius A, Ganesan V (2006) *Langmuir* 22:469–477
- Ganesan V, Walcarius A (2008) *Mater Sci Eng B* 149:123–132
- Pal M, Ganesan V (2012) *Catal Sci Technol* 2:2383–2388
- Pal M, Ganesan V, Azad UP (2012) *Thin Solid Films* 525:172–176
- Sartori G, Bigi F, Maggi R, Sartorio R, Macquarrie DJ, Lenarda M, Storaro L, Coluccia S, Martra G (2004) *J Catal* 222:410–418
- Benhamou A, Baudu M, Derriche Z, Basly JP (2009) *J Hazard Mater* 171:1001–1008
- Chong ASM, Zhao XS (2003) *J Phys Chem B* 107:12650–12657
- Kisler JM, Gee ML, Stevens GW, O'Connor A (2003) *Chem Mater* 15:619–624
- Zhang X, Zhang C, Guo H, Huang W, Polenova T, Francesconi LC, Akins DL (2005) *J Phys Chem B* 109:19156–19160
- Mani V, Wu TY, Chen SM (2014) *J Solid State Electrochem* 18:1015–1023
- Zen JM, Kumar AS, Wang HF (2000) *Analyst* 125:2169–2172
- Ojani R, Raof JB, Zamani S (2013) *Appl Surf Sci* 271:98–104
- Cardoso WS, Gushikem Y (2005) *J Electroanal Chem* 583:300–306
- Jing L (2009) *Chin J Chem* 27:2373–2378
- He Q, Gan T, Zheng D, Hu S (2010) *J Solid State Electrochem* 14:1057–1064
- Menezes EWD, Nunes MR, Arenas LT, Dias SLP, Garcia ITS, Gushikem Y, Costa TMH, Benvenutti EV (2012) *J Solid State Electrochem* 16:3703–3713
- Ganesan V, Pal M, Tiwari M (2014) *Bull Mater Sci* 37:623–628
- Frenzel W, Brussel JS, Zinvirt B (2004) *Talanta* 64:278–282
- Chen ZF, Jiang YX, Xu YWJM, Jin LY, Sun SG (2005) *J Solid State Electrochem* 9:363–370
- Rai A, Singh A, Ahmad A, Sastry M (2006) *Langmuir* 22:736–741
- Morais AD, Silveira G, Villis PCM, Maroneze CM, Gushikem Y, Pissetti FL, Lucho AMS (2012) *J Solid State Electrochem* 16:2957–2966
- Stamplecoskie KG, Scaiano JC (2010) *J Am Chem Soc* 132:1825–1827
- Encai H, Schatza GC (2004) *J Chem Phys* 120:357–366
- Zhu J, Liu S, Palchik O, Koltypin Y, Gedanken A (2000) *Langmuir* 16:6396–6399
- Xue Z, Zhang F, Qin D, Wang Y, Zhang J, Liu J, Feng Y, Lu X (2014) *Carbon* 69:481–489
- Yu JJ, Lu S, Li JW, Zhao FQ, Zeng BZ (2007) *J Solid State Electrochem* 11:1211–1219
- Han X, Zhu Y, Yang X, Zhang J, Li C (2011) *J Solid State Electrochem* 15:511–517
- Hemant NKS, Kumar G, Karthik L, Bhaskara R KV (2010) *Arch Appl Sci Res* 2:161–167
- Chen YC, Young RJ, Macpherson JV, Wilson NR (2007) *J Phys Chem C* 111:16167–16173
- Xiaohui L, Li Y, Wei C, Yan T, Li Y, Du B, Wei Q (2014) *Sensors Actuators B* 202:53–59
- Mukherjee P, Patra CR, Ghosh A, Kumar R, Sastry M (2002) *Chem Mater* 14:1678–1684
- Jaroniec CP, Kruk M, Jaroniec M, Sayari A (1998) *J Phys Chem B* 102:5503–5510
- Jaroniec CP, Gilpin RK, Jaroniec M (1997) *J Phys Chem B* 101:6861–6869
- Caro CA, Bedioui F, Zagal JH (2002) *Electrochim Acta* 47:1489–1494
- Kamyabi MA, Aghajani F (2008) *J Electroanal Chem* 614:157–165
- Matemadombo F, Nyokong T (2007) *Electrochim Acta* 52:6856–6864
- Lin CY, Vasantha VS, Ho KC (2009) *Sensors Actuators B* 140:51–57
- Nitrate and nitrite in drinking-water, background document for development of WHO guidelines for drinking-water quality (2003) WHO. http://www.who.int/water_sanitation_health/dwq/chemicals/nitratennitrite2ndadd.pdf
- Dionex product manual (2010) Thermo fisher scientific. http://www.dionex.com/en-us/webdocs/113697-AU185-IC-Nitrate-Nitrite-Wastewater-06Aug2012-AU70208_E.pdf
- Yang C, Xu J, Hu S (2007) *J Solid State Electrochem* 11:514–520
- Sljukic B, Banks CE, Crossley A, Compton RG (2007) *Electroanalysis* 19:79–84
- Zhao K, Song H, Zhuang S, Dai L, He P, Fang Y (2007) *Electrochem Commun* 9:65–70
- Nie T, Zhang O, Lu L, Xu J, Wen Y, Qiu X (2013) *Int J Electrochem Sci* 8:8708–8718
- Azad UP, Turllapati S, Rastogi PK, Ganesan V (2014) *Electrochim Acta* 127:193–199
- Mani V, Periasamy AP, Chen SM (2012) *Electrochem Commun* 17:75–78
- Feng JJ, Zhang PP, Wang AJ, Zhang Y, Dong WJ, Chen JR (2011) *J Colloid Interface Sci* 359:1–8
- Zheng D, Hu C, Peng Y, Hu S (2009) *Electrochim Acta* 54:4910–4915
- Sahindokuyucu MF, Erdogan N (2010) *J Anim Vet Adv* 9:2013–2016